Meccanica (2015) 50:549–560
DOI 10.1007/s11012-014-9950-9

EXPERIMENTAL SOLID MECHANICS

Multiphysics design and implementation of a microsystem for displacement-controlled tensile testing of nanomaterials

Maria F. Pantano · Rodrigo A. Bernal · Leonardo Pagnotta · Horacio D. Espinosa

Received: 11 July 2013 / Accepted: 8 April 2014 / Published online: 30 April 2014

Abstract MEMS-based tensile testing devices are powerful tools for mechanical characterization of nanoscale materials. In a typical configuration, their design includes an actuator to deliver loads/displacements to a sample, and a sensing unit for load measurement. The sensing unit consists of a flexible structure, which deforms in response to the force imposed to the sample. Such deformation, while being necessary for the sensing function, may become a source of instability. When the sample experiences a load drop, as it may result from yield, necking or phase transitions, the elastic energy accumulated by the sensor can be released, thus leading to loss of the displacement-controlled condition and dynamic failure. Here, we report a newly-developed MEMS testing system where the sensor is designed to constantly keep its equilibrium position through an electrostatic feedback-control. We show design, implementation, and calibration of the system, as well as validation by tensile testing of silver nanowires. The implemented system allows capture of softening events and affords significant improvement on the resolution of stress–strain curves.

Keywords MEMS · SEM · In-situ · Mechanical characterization · Feedback control · Nanowires

1 Introduction

Development of accurate metrology is critical to characterize unambiguously the extraordinary mechanical, electrical, and optical properties of nanostructures, such as nanowires and nanotubes, which are envisioned as the building blocks of the next generation of electronic devices [1, 2]. However, the size of nanostructures, while being the key to their unique behavior, significantly affects the capability of manipulation and testing with conventional techniques [3, 4]. As a result, numerous dedicated systems have been developed for testing microscale and nanoscale 2D and 1D structures [5–13]. Among these methodologies, Microelectromechanical System (MEMS)-based techniques are preferred [14, 15] because they allow carrying out in situ testing in Scanning and Transmission Electron Microscopes (SEM/TEM). These in situ techniques allow for real-time imaging and structural characterization of sample deformation, thus facilitating the determination of structure–property relations.

Maria F. Pantano and Rodrigo A. Bernal have contributed equally to this work.

M. F. Pantano · L. Pagnotta
Department of Mechanical Engineering, University of Calabria, Ponte P. Bucci, 44C, 87036 Rende, Italy

R. A. Bernal · H. D. Espinosa (✉)
Department of Mechanical Engineering, Northwestern University, 2,145 Sheridan Road, Evanston, IL 60208, USA
e-mail: espinosa@northwestern.edu

MEMS-based testing systems typically consist of an actuator (to apply loads/displacements) and a sensor, whose deformation during a test can be related to the force experienced by the sample. Two main configurations are typical, depending on how the sensor is positioned with respect to the sample. In the first case, the sample is placed between the actuator and the sensor [8, 12, 16, 17], and both are subjected to the same load. In the second case, the specimen load is derived by comparing the displacement of a flexible sensing structure (e.g., the thermal actuator in [10], or a system of springs in [6]) with and without a sample under the same actuation conditions. In both cases, instability phenomena may occur when the sample exhibits stress relaxation (decrease in engineering-stress), as it may result from yield, necking or phase transitions [18, 19]. In the first device type (sensor and sample experience the same load), when the specimen requires less force to be further deformed, part of the elastic energy accumulated by the sensor during the test is released and the specimen is pulled by the sensor, leading to loss of the displacement-control condition. In the second device type, the presence of a sample decreases the displacement of the sensor. In case of stress relaxation in the specimen, the force required for further deformation decreases, and, consequently, the sensor deforms more, trending to the displacement achieved without a sample. Thus, the displacement-controlled condition can also be lost.

Similar observations were reported several years ago in mechanical testing at the macroscale. Yield drops [20], and high and low yield points [21] were better captured in "hard" (or stiff) testing machines, a "hard" machine having a spring constant much larger than that of the specimen, and therefore closer to a displacement-control condition. Higher elongation at fracture, and transition from brittle to ductile fracture were observed by testing the same material in a "hard" machine, instead of a "soft" one [22], although strain at fracture is also influenced by the aspect ratio of the specimen [23, 24]. Ultimately, these differences seem to arise from the elastic energy stored, either in the testing machine or the specimen itself, and how it is released during a stress relaxation or load drop [24].

A MEMS device for 1D nanomaterial testing can be made into a "hard" machine if the load sensor is forced to remain stationary. However, the load sensor loses its sensing function, and other methodology instead of that based on its deformation has to be adopted for force measurement. A possible strategy, here pursued, involves a feedback control scheme, able to keep the sensor in its equilibrium position, regardless of what happens to the sample, while providing an electronic measurement of the force. Feedback control has already found application in a variety of MEMS devices, as accelerometers [25], gyroscopes [26], micromirrors [27], actuators [28], and positioners [29]. Here, we designed and implemented such scheme into a novel MEMS for displacement-controlled tensile testing of 1D nanostructures.

2 Device concept and design

A schematic of the device concept and how displacement control was achieved is shown in Fig. 1. The system is conceptually similar to a previous design [11, 16, 30, 31], where a thermal actuator applies displacement to the specimen and a capacitive displacement sensor with a known spring constant (herein referred to as "load sensor") is used to measure the force. However, in order to achieve displacement control at both sides of the specimen, an electrostatic actuator was added in the far end of the load sensor. This addition required new designs, validation and fabrication technology, compared to previous implementations.

The operation of the device is as follows. When a voltage is applied across the v-shaped beams of the thermal actuator, current flow generates Joule heating, causing deformation of the beams, which in turn move a shuttle, where the specimen is attached. This actuator is designed for displacement control, i.e. its displacement is the same regardless of the stiffness of the specimen connected to it (see Sect. 2.1). On the other side, the sample is connected to a capacitive displacement sensor. This is an interdigitated-finger sensor [31], where a capacitance difference proportional to the displacement is generated and then measured by an electronic scheme, which ultimately produces a voltage proportional to the displacement.

The electrostatic actuator applying force in the far end of the load sensor allows achieving displacement control in both ends. The feedback control operation can be understood in the following manner. When the thermal actuator is biased with a voltage, a part of the delivered displacement is transferred through the sample to the load sensor, which then moves away

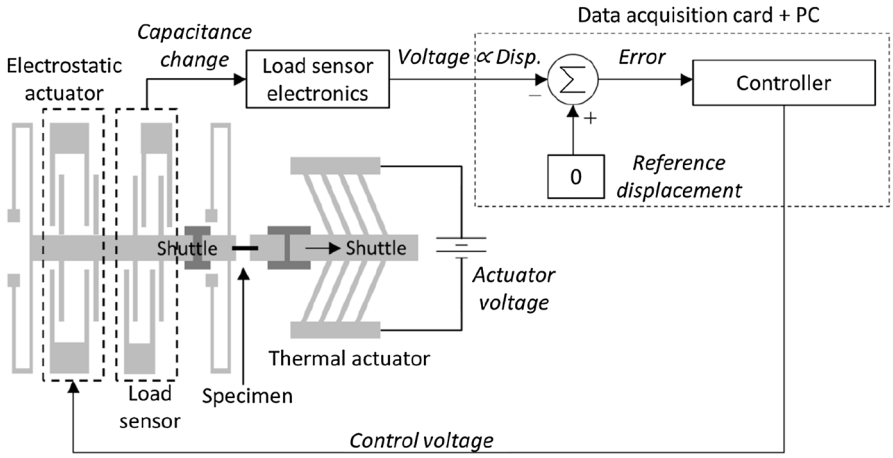

Fig. 1 Schematic of the closed-loop scheme implemented in the device for feedback control of the displacement sensor. Signals are in italics

from its initial position. As a consequence, the output voltage from the load sensor electronics varies in proportion to the load sensor displacement. This voltage is acquired and compared to a reference voltage, corresponding to the equilibrium condition (i.e., displacement = 0). The difference between them (error) is provided as input to a controller, which computes the voltage to be applied to the electrostatic actuator, in order to restore zero displacement of the load sensor. While the description given here is sequential, the electronic system works in real time, resulting in a steady equilibrium position of the load sensor regardless of the applied force. When the device operates in this fashion, hereon referred to as "closed-loop mode", the displacement sensor output, being zero (e.g., corresponding to no displacement), cannot longer be used for quantification of the force in the specimen. However, this force is equal to the force applied by the electrostatic actuator, which can then be inferred from the applied voltage and the actuator geometry.

2.1 Thermal actuator design

The thermal actuator design was carried out based on two parameters: the maximum displacement it can deliver (d_A), and its axial stiffness (k_A). The stiffness should be higher than the equivalent stiffness of the sample, in order to ensure displacement control in the actuator end of the specimen [30]. This effect can be evaluated as:

$$\frac{u_d}{u_u} = \frac{1}{1 + \frac{k_C}{k_A}}, \tag{1}$$

where u_u is the actuator displacement without any sample, u_d is its displacement with a sample, and k_c is the combined stiffness of the specimen and the load sensor (they are treated as springs in series). In order for the thermal actuator to move by the same amount even when there is a sample, the ratio k_C/k_A should be as small as possible. In particular, if $k_A = 100k_c$, then $u_d = 99\ \%u_u$, which guarantees that tests are effectively conducted under displacement control. With reference to the sample, its stiffness can simply be evaluated as $k_s = EA/L$, where E is the Young modulus, A the transverse area, and L the length. The stiffness of the load sensor is determined by the geometry of the supporting folded beams, and is typically designed to be similar to the specimen's stiffness. If $k_A > 20{,}000$ N/m, the thermal actuator is suitable to test a variety of materials with either relatively low (e.g. 80 GPa for silver [32]) or high (e.g. 300 GPa for gallium nitride [33]) Young's modulus, while preserving displacement control.

The second parameter is the maximum actuator displacement, which must be sufficiently high (~ 1 μm) to fracture a variety of samples. We consider the analytical models derived in [30], which relate stiffness and displacement to the actuator geometry and material:

$$k_A = 2N\left(\sin^2\alpha\frac{EA}{L} + 12\frac{EI}{L^3}\cos^2\alpha\right) \tag{2}$$

Table 1 Physical properties of single-crystal silicon used in the multiphysics simulation

Young modulus (GPa)	$E_x = E_y = 169$; $E_z = 130$ [35]
Poisson ratio	$\nu_{yz} = 0.36$; $\nu_{zx} = 0.28$; $\nu_{yz} = 0.064$ [35]
Shear moduli (GPa)	$G_{yz} = G_{zx} = 79.6$; $G_{xy} = 50.9$ [35]
Thermal expansion coefficient (K^{-1})	$\alpha(t) = (3.725\{1-\exp[1-5.88 \times 10^{-3}(t-124)]\} + 5.548 \times 10^{-4}t) \times 10^{-6}$ [36]*
Density (kg/m^3)	2,330 [37]
Resistivity (Ωm)	1.3×10^{-4} [38]
Thermal conductivity ($Wm^{-1}K^{-1}$)	130 [37]

* t is the absolute temperature expressed in [K]

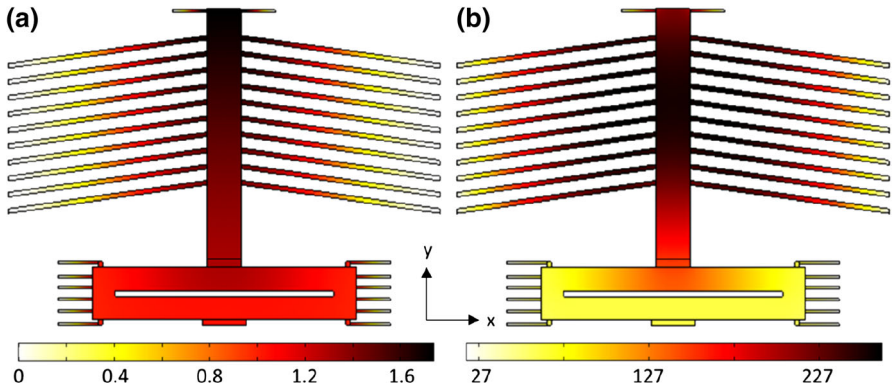

Fig. 2 Results from an electro-thermal–mechanical analysis in terms of **a** displacement [μm] and **b** temperature [°C] when biasing the thermal actuator with 7 V

$$u_u = \frac{\alpha \Delta T L \sin\alpha}{\sin^2\alpha + 12\frac{I}{AL^2}\cos\alpha}, \quad (3)$$

where α is the inclination angle of the v-shaped beams, ΔT is the temperature increase, L is the length, I is the inertia moment, A is the transverse area, E is the Young modulus, and N is the number of the beams.

According to Eqs. (2) and (3), when considering 10 v-beams with length of 350 μm, width of 8 μm, and thickness of 25 μm, the axial stiffness and the maximum displacement are 38,400 N/m and 6.4 nm/ °C, respectively. Such values guarantee structural integrity with respect to bending and buckling loads and satisfy both the requirements of high stiffness and high displacement defined above.

Beyond the series of v-beams, it is necessary to include in the thermal actuator design another structure to improve heat dissipation [30, 34], and thus decrease the temperature change within the specimen. This design was evaluated through electro-thermal-structural analysis, performed in COMSOL Multiphysics software, with the physical parameters listed in Table 1.

Figure 2 shows the temperature and the displacement field at 7 V on the final design, which includes a hollow rectangle, clamped to the substrate through 12 short beams (60 μm long, 4 μm wide, and 25 μm thick).

The displacement at the interface with the specimen (bottom surface of the actuator) is greater than 1 μm, while the temperature is about 65 °C, which is significantly lower (only 25 %) than the temperature on the actuator shuttle. The short beams provide heat dissipation by conduction through the substrate. Conduction is the main heat dissipation mechanism since for in situ experiments in SEM or TEM the thermal actuator works in vacuum, corresponding to no convection. Consequently, the higher the number of anchor points, the more efficient is the heat dissipation. In addition, the rectangular dissipating structure increases the electrical resistance, thus further limiting the temperature increase [34].

2.2 Electrostatic actuator

The electrostatic actuator was designed with 12 finger-pairs for actuation. The width of these fingers, in the movable and fixed parts, is significantly larger than that of the sensing fingers. This guarantees that high

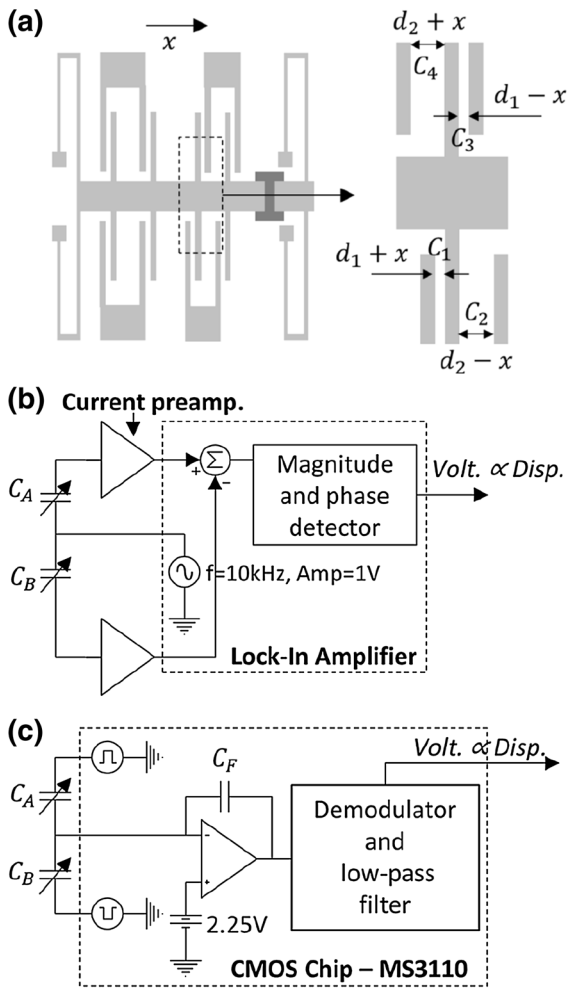

Fig. 3 **a** Schematic of the load sensor. **b** The lock-in amplifier based circuit for detection of the capacitance across the displacement sensor branches. **c** The CMOS-based architecture for capacitance detection

voltages applied to the actuator result in motion of the sensor shuttle, and not in mutual pull-in of the finger pairs. When a voltage is applied across the fixed and moving electrodes, the net electrostatic force (F_{LSA}) can be calculated as:

$$F_{LSA} = \frac{1}{2}\varepsilon M \frac{A}{d^2} V^2, \tag{4}$$

where ε is the permittivity, M (= 12) the number of electrodes, A their transversal area (= 200 × 25 μm^2), d(= 2.6 μm) the gap between two adjacent electrodes, and V the effective bias voltage, which is the voltage in the actuator minus the voltage in the sensor shuttle.

The surface micromachining fabrication process adopted for previous device generations allowed for structures with thickness of about 3.5 μm [16], which was found insufficient to generate enough electrostatic force under moderate voltages, due to a small area term A. Thus, it was necessary to implement the new device using an SOI (Silicon-On-Insulator) process, which allows for a device thickness of 25 μm. When biasing the actuator at 38 V, the current design allows an electrostatic force of about 95 μN, which is sufficient to bring to fracture a variety of 1D nanostructures.

2.3 Load sensor design and electronics

The load sensor included in the device is based on a differential capacitive scheme (Fig. 3a), which provides a quasi-linear relationship between displacement and the corresponding capacitance variation [11]. The configuration previously adopted using surface micromachining [16] could not be reproduced in this case because of SOI fabrication features. Previously, each moving finger laid between two stationary electrodes, requiring more layers of connectivity, readily provided by surface micromachining. In SOI technology, the device and connection layers are the same, limiting the complexity of the structure. Thus, an alternative solution [8], was considered. In this case, only one set of fixed fingers is implemented in either side of the sensor. Conceptually, the operating principle remains the same.

A displacement x of the sensor shuttle causes a capacitance difference between its two branches (A and B) of N number of fingers equal to [39]:

$$\begin{aligned}\Delta C = C_A - C_B &= N(C_3 + C_4) - N(C_1 + C_2)\\ &= N\varepsilon A\left[\frac{1}{d_1 - x} + \frac{1}{d_2 + x}\right]\\ &\quad - N\varepsilon A\left[\frac{1}{d_1 + x} + \frac{1}{d_2 - x}\right]\end{aligned} \tag{5}$$

Considering $d_1 \ll d_2$ ($d_1 = 2$ μm and $d_2 = 20$ μm) and $x \ll d_1$, Eq. (9) simplifies to:

$$\Delta C = 2N\varepsilon A \frac{x}{d_1^2} \tag{6}$$

In the present configuration, the comb-drive elements (17 on each side) are designed to be 200 μm long, 25 μm thick, thus providing a theoretical

sensitivity $S = 0.38$ fF/nm, which is about one order of magnitude higher than previously reported [16], and comparable to that in [8].

The capacitance difference (ΔC) between the sensor branches can be detected through two different electrical circuits, involving either a commercial CMOS chip [16] or a lock-in amplifier [40]. Here, we conducted a study to compare the performance of both systems, due to reports in the literature [40] which suggested a better performance with the lock-in system.

In the lock-in amplifier scheme (Fig. 3b), an AC signal is connected to the sensor shuttle, thus causing an AC current to flow through both branches. Each branch of the sensor, representing a variable capacitor, is connected to a current pre-amplifier (model 1212, DL Instruments, LLC). The outputs of the two current pre-amplifiers are fed into a lock-in amplifier (model SR830, SRS), which operates in differential mode. The output voltage from the lock-in amplifier can be computed as [40]:

$$V_{\text{lock-in}} = \frac{G2\pi f V_{\text{ref}}}{\sqrt{2}} \Delta C, \tag{7}$$

where G is the pre-amplifiers gain (10^6 V/A), $f = 10$ kHz, and $V_{\text{ref}} = 1$ V, are the frequency and the amplitude of the AC reference voltage applied through the lock-in amplifier to the sensor shuttle, and $\sqrt{2}$ is the RMS conversion factor.

On the other hand, the commercial CMOS Chip (MS3110, Irvine Sensors, CostaMesa, CA) [16] applies a square, opposite–phase signal to both branches of the sensor. The amplitude of the voltage in the shuttle is proportional to the capacitance change and its phase indicates the direction of movement. This signal is amplified and demodulated inside the chip, yielding a DC voltage proportional to the capacitance variation. The output voltage is:

$$V_{\text{CMOS}} = 2.565 \frac{G_{\text{CMOS}} \Delta C}{C_{\text{F}}} + 2.25 \tag{8}$$

The parameters in this equation were programmed in the chip as $G_{CMOS} = 2$ (Gain), $C_F = 1.2825$pF (feedback capacitor).

3 Device fabrication

As previously mentioned, the present device was fabricated through an SOI process (SOIMUMPs) where the silicon structural layer is 25 μm thick. The process was carried out in a commercial foundry (MEMSCAP, NC). With respect to the standard process flow, custom steps were implemented in order to achieve electrical isolation between the actuator and sensor, and the areas where the sample is placed. This improvement has two main advantages. First, coupled electromechanical measurements can be potentially carried out. Second, given that the electron beam in SEM or TEM impinges the specimen area, isolating the actuating and sensing part of the device from this region avoids any artifact introduced by the electron beam in the measurements. In fact, preliminary measurements performed with a device without this isolation, using the lock-in amplifier sensing scheme, showed a constant drift of the sensor signal when the electron beam was imaging the specimen. Incidentally, note that spurious effects in the measured electrical characteristics of Si nanowires, when imaged under SEM, were reported in [7].

The steps of the fabrication process [41] are listed below and shown in Fig. 4a:

1) Doping of the silicon structural layer through deposition of a layer of PSG (phosphosilicate glass);
2) First metal deposition for definition of connection pads and traces;
3) Patterning of the silicon structural layer through DRIE (Deep Reactive Ion Etching);
4) Deposition of a protective layer on the silicon structural layer;
5) Partial etching of the silicon substrate (additional step with respect to the standard SOIMUMPS flow);
6) Patterning of the silicon substrate by DRIE, while the silicon structural layer is still covered by the protective layer;
7) Removal of the protective layer and release of the freestanding structures on the silicon structural layer;
8) Second metal deposition for definition of metal features with coarser tolerance.

The fabricated device is shown in Fig. 4b.

4 Device characterization

After fabrication, calibration tests were performed on the thermal actuator, electrostatic actuator and load

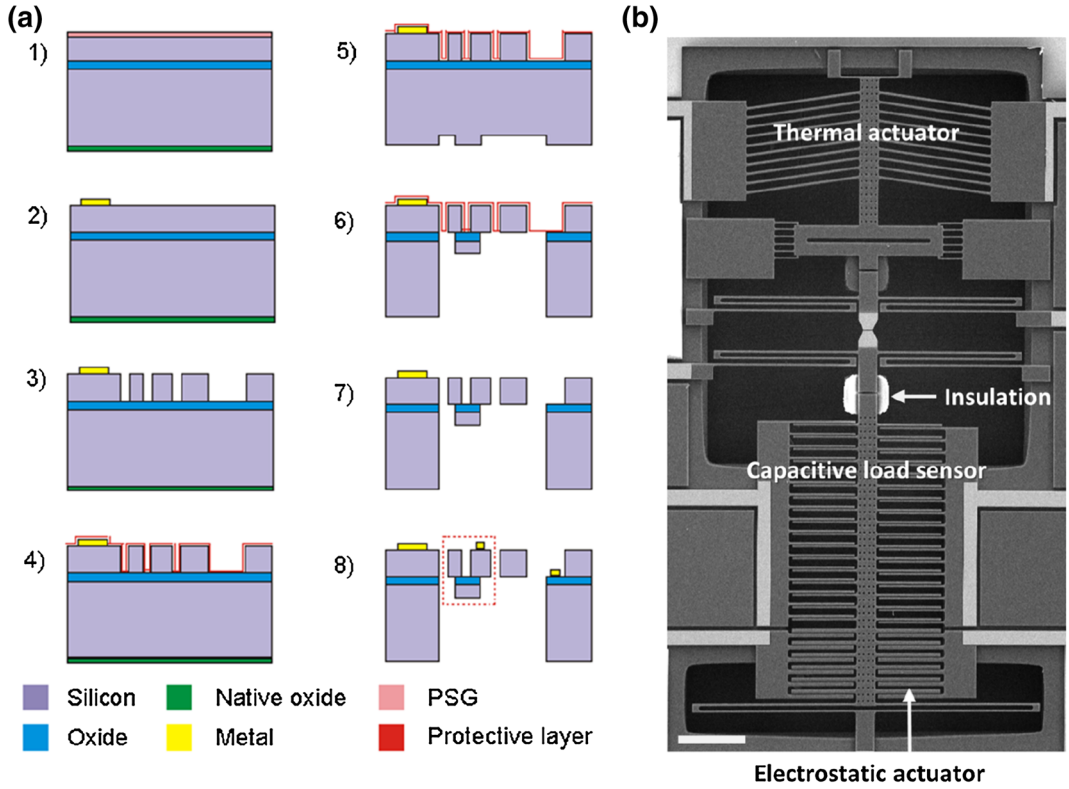

Fig. 4 **a** Steps of SOI fabrication process. 1) Doping of the silicon structural layer; 2) First metal deposition; 3) Etching of the silicon structural layer; 4) Deposition of a protective layer on silicon; 5) Partial etching of the substrate; 6) Final etching of the substrate; 7) Release of the freestanding structures; 8) Second metal deposition. The dashed box highlights the freestanding structures, which are electrically isolated while still mechanically connected. **b** SEM micrograph of the fabricated device. Scale bar 200 μm

sensor in order to compare the device performances to the designed behavior.

4.1 Thermal actuator

Displacements were generated by a DC bias voltage applied to the actuator while all the other structures were grounded and no specimen was present. At each voltage, a picture of the gap between the thermal actuator and the load sensor was processed through a MATLAB custom-made DIC (Digital Image Correlation) code for determining the displacement. The displacement-voltage curves obtained through multi-physics numerical analyses and experiments show good agreement in the whole range (Fig. 5a).

The thermal actuator calibration curve is useful during tests, allowing deriving its displacement in real time from the bias voltage. Since the actuator has a high stiffness, the displacement of the actuator is not affected by the presence of a sample. Note that the voltage waveform applied to the actuator during calibration is the same as the one applied during specimen testing.

4.2 Electrostatic actuator calibration

A DC voltage was applied between the stationary and moving electrodes of the actuator, while keeping grounded all the other structures. The resulting displacement was obtained using the same methodology as that employed in the thermal actuator calibration.

At each step, the actuator/sensor shuttle reached an equilibrium position, thus requiring the sum of the forces acting on it (electrostatic and elastic) to be zero:

$$k_{EA} \cdot x = \frac{1}{2} M \varepsilon \frac{A}{(d_0 - x)^2} V^2, \tag{9}$$

where k_{EA} is the elastic constant of the supporting beams, which is 20 N/m in the present design. By solving this non-linear equation for x, the

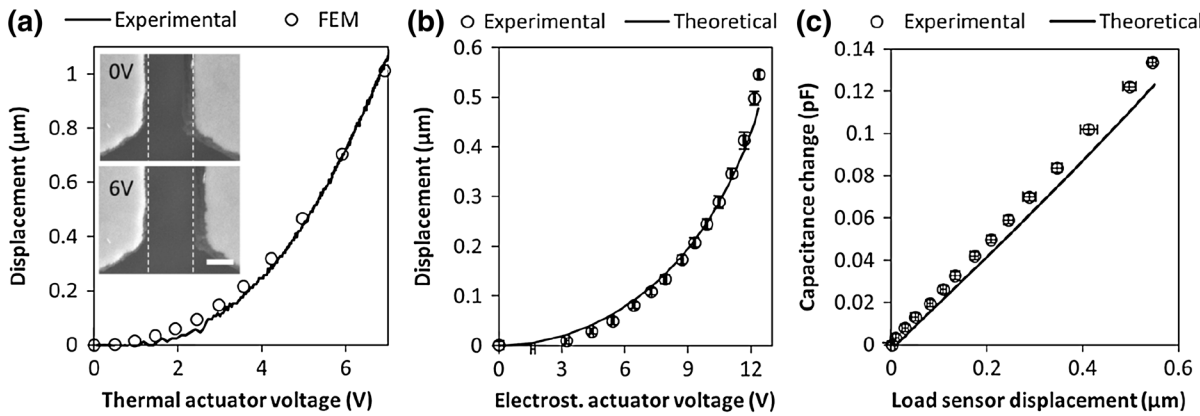

Fig. 5 **a** Calibration of the thermal actuator, comparing between experimental and numerical data. Inset shows the type of images of the shuttles used to measure the displacements. Scale bar: 1 µm. **b** Comparison between the theoretical and experimental displacement of the electrostatic actuator. **c** Comparison between the capacitance change-displacement relationship determined both analytically and experimentally for the load sensor

displacement corresponding to each value of the bias voltage V can be determined. Such analytical values are in good agreement with the data derived by experiments, as shown in Fig. 5b.

4.3 Load sensor calibration

For testing the load sensor, a displacement was imposed through the electrostatic actuator, while the thermal actuator was grounded, and the sensor electrodes were connected to either one of the capacitive-sensing schemes explained in Fig. 3b, c.

At each step, the shuttle displacement was derived from SEM images. The experimental capacitance difference was derived from a measurement of the output voltage of the capacitive sensing circuit. Figure 5c shows a comparison between the experimental and analytical relationship of capacitance variation versus displacement. A good agreement is observed between them, with a slight difference at large displacement which can be related to nonlinearities occurring in the large-displacement range. Note however, that during closed-loop operation, the load sensor remains very close to the zero-displacement position.

5 Implementation and calibration of the feedback control

Data acquisition is performed through LABVIEW software, and a data acquisition (DAQ) card (NI USB-6009). A fast-response (100 kHz) analog controller (Stanford Research SIM960) is used to calculate and generate the feedback voltage. This voltage (0–5 V range) is then amplified (Texas Instruments OPA 445) to allow application of the higher voltages needed to balance the specimen's forces.

Different analog control architectures were considered. For simplicity, a proportional controller was implemented in preliminary experiments. It was found that the proportional constants necessary to maintain the steady-state error below 50 nm causes instability in the plastic regime when testing silver nanowires. Thus, later experiments were carried out using a proportional-integral-derivative (PID) controller. The main advantage of the PID is the ease of implementation and tuning.

The output signal *u(t)* of a basic PID controller is [42]:

$$u(t) = k_P\left[e(t) + \frac{1}{T_i}\int_0^t e(\tau)d\tau + \frac{1}{T_d}\frac{d}{dt}e(t)\right], \qquad (10)$$

where *e(t)* is the error signal (see Fig. 1), provided as input to the controller, k_p, T_i, and T_d are the proportional, integral, and derivative constants, which define the controller. Such parameters were determined through the Ziegler-Nichols method [42], in which the step response of the open-loop system has to be first studied. In the open-loop scheme, the system is excited by a step signal, generated by a voltage applied to the electrostatic actuator.

In Fig. 6a, we present a comparison of the response to a voltage step at $t = 10$ s of the two alternative

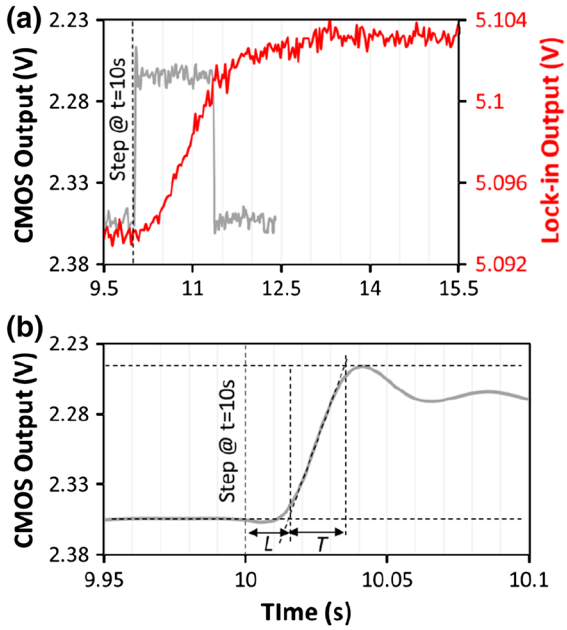

Fig. 6 **a** Step response (step at $t = 10$ s) of the open-loop scheme, using the two alternatives for capacitive sensing. **b** Detail of the CMOS open-loop step response for definition of the PID parameters. Note that in both plots the CMOS output was inverted to ease comparison with the lock-in signal

schemes for capacitive sensing. The lock-in amplifier requires about 3.5 s to fully respond, while the CMOS scheme responds significantly faster ($\sim$40 ms), allowing removal of the voltage step within a very short period of time (Fig. 6b).

The dramatic difference in response time likely arises from the fact that the CMOS system can be integrated with the MEMS device much more closely. On the other hand, the lock-in system, which involves several instruments, requires long cables that introduce capacitive coupling and potential noise. The lock-in amplifier eliminates this noise trough averaging, at the expense of response time. Given these results, the CMOS scheme was considered a better alternative for the implementation of the controller.

Using the Ziegler-Nichols tuning method (Fig. 6b) two parameters can be identified from analysis of the point of inflection of the CMOS step response, the delay time L (15 ms) and the time constant T (20 ms). These parameters are used to derive the constants of the controller as follows [42]:

$$k_p = 1.2\frac{T}{L} = 1.33 \tag{11}$$

$$T_i = 2L = 0.03s \tag{12}$$

$$k_d = 0.5L = 0.0075s \tag{13}$$

6 Mechanical testing of silver nanowires

In order to validate the system, we carried out in situ SEM mechanical testing of penta-twinned silver nanowires. The experiments were carried out in a FEI Nova Nano 600 SEM. The very same batch of nanowires was tested in situ TEM using our previous generation of devices [32]. Thus, its properties are well known and a validation of the new system can be carried out.

Below, we report two representative tests of similar-diameter nanowires (118 nm). To better showcase the benefits afforded by testing with displacement control, we aim to contrast this scheme against force control testing, in which the feedback control is not enabled and the load sensor deforms from its equilibrium position. To that end, we test a 118 nm in displacement control and compare the results with measurements of a nanowire of the same diameter tested in force control in our previous study [32]. The nanowires were mounted on the MEMS using a nanomanipulator (Klocke Nanotechnik), and fixed by e-beam induced Platinum deposition [43].

During the displacement control test, the voltage applied to the thermal actuator was increased in a monotonic, continuous fashion through a programmed waveform from a signal generator, in order to obtain a constant thermal actuator displacement rate (speed). In a separate experiment with a different nanowire, validation of the correct functioning of the controller was established by comparing nanowire deformation (obtained from SEM pictures) and the thermal actuator displacement, calibrated in the same experiment before the specimen was mounted on the device (Fig. 7). These two quantities are similar within experimental error, thus ensuring that during the test, the load sensor does not move more than 20 nm from the equilibrium position and displacement control was maintained. The strain in the nanowire can then be determined either from SEM images, or from the voltages recorded for the thermal actuator and the load sensor.

Figure 8 shows the stress–strain curves of the nanowires. For details on data reduction related to the

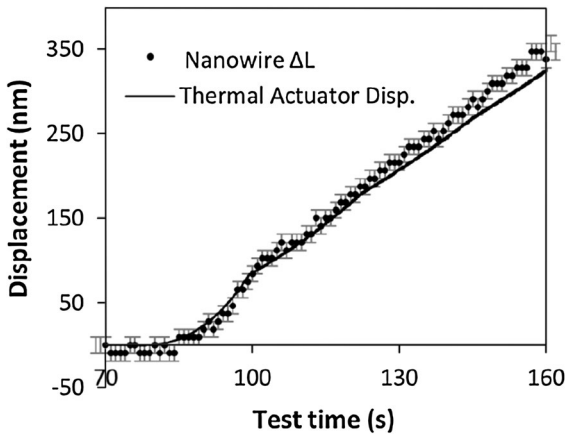

Fig. 7 Nanowire displacement compared to the expected thermal actuator displacement during the test

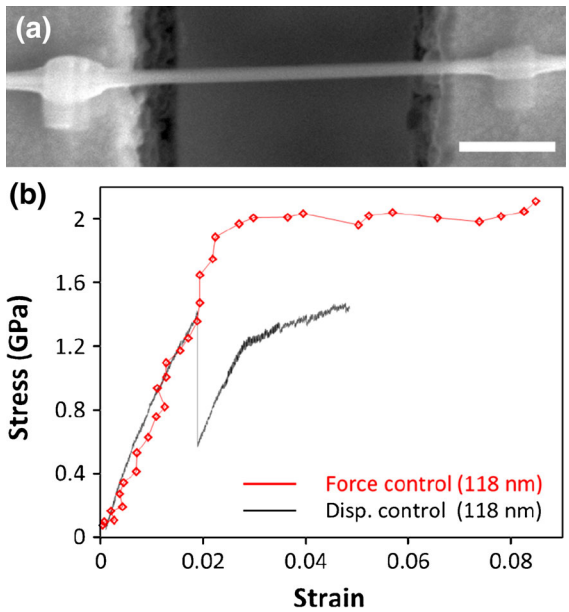

Fig. 8 **a** 118 nm silver nanowire tested in displacement control. **b** Comparison of the stress–strain curves obtained in force control and displacement control. Force control data from [32]

force control curve see [32]. In the displacement control case, the strain was derived from the electronic signals of the thermal actuator and load sensor voltages, the data acquisition rate was 1,000 Hz, and a moving average filter with a window of 20 data points was applied to filter out noise. The force is derived from the control voltage applied to the electrostatic actuator and Eq. (4). The force is divided by the initial nanowire cross-section, which was assumed to be of circular shape [32]. The diameter was determined by a high-resolution image of the nanowire.

The wire tested in displacement control displays elastic behavior up to 1.9 % strain, followed by a drastic stress relaxation or load drop. This drop is associated with yield and an avalanche process in which many dislocations are nucleated [32]. Note that this yield drop has been observed previously in molecular dynamics simulations of penta-twinned silver nanowires [19, 32, 44], as well as in other penta-twinned FCC nanowires [45, 46]. Following the yield drop, reloading occurs and the nanowire undergoes mild strain hardening up to failure. In contrast, this level of detail is not captured in the force control scheme. In this case, dislocation nucleation events are captured as plateaus or strain-bursts [19]. These bursts are caused by a sudden release of elastic energy from the load sensor, which springs back due to the rapid decrease in the load that the nanowire is bearing as it undergoes yielding [18].

This comparison therefore shows that displacement control testing is advantageous to capture sudden softening events, in this case associated with yield. However, other effects where sudden load drops are expected, for example phase transitions, can potentially be captured [18]. Note also that the implementation of feedback control has the beneficial effect of vastly improving the signal to noise ratio of the stress–strain curve. This improvement arises because the load is derived from the control voltage, which is of the order of several Volts, as opposed to the force control scheme, in which the load is derived based on the load sensor signal, which has a range on the order of mili-Volts [11].

7 Conclusions and future developments

In summary, we designed and implemented a MEMS device and associated electronics for displacement-controlled, in situ tensile testing of 1D nanomaterials. The system has several advantageous features. Because of the high stiffness of the thermal actuator, displacements can be derived in real-time from the bias voltage, which can be converted into displacement through a calibration curve. Applied loads can be derived from the voltage applied to an electrostatic

actuator through a feedback control loop. The implementation of the feedback control prevents the device sensor from any significant displacement, thus removing a potential source of instability when load drops in the specimen occur.

Experimental calibration of the present device showed very good agreement with the expected behavior. The comparison between CMOS and lock-in-based methods of load-sensing revealed a vastly superior time response of the CMOS, probably a result of the closer integration between the CMOS and the MEMS inside the SEM chamber.

The system was validated through in situ SEM tensile testing of silver nanowires and comparison with force control testing. A yield drop in the specimen, predicted by molecular dynamic simulations, which previously could not be captured in force control schemes, was observed. This comparison demonstrates the potential of the displacement-controlled system to capture load relaxation events such as yield drops or phase transitions.

Future work will focus on capturing stable necking, up to fracture, of nanowires. Such fracture not only requires displacement control (a "hard" machine), as implemented here, but also control of the aspect ratio of the specimen [23, 24]. Although load drops corresponding to fracture initiation or necking were not recorded, a yield drop was clearly observed in the intermediate portion of the curve. Significant necking may not be possible in the penta-twinned nanowires tested here, but may emerge in single-crystal nanowires. In conclusion, the development of full displacement control tensile testing of nanowires adds another dimension to the existing toolbox for nanomaterial testing, and is expected to yield further insights into nanoscale behavior, especially of metallic nanostructures.

Acknowledgments H.D.E. gratefully acknowledges support from NSF through award No. DMR-0907196.

References

1. Dasgupta NP, Sun J, Liu C, Brittman S, Andrews SC, Lim J, Gao H, Yan R, Yang P (2014) 25th Anniversary article: semiconductor nanowires – synthesis, characterization, and applications. Adv Mater 26:2137
2. Yan H, Choe HS, Nam SW, Hu YJ, Das S, Klemic JF, Ellenbogen JC, Lieber CM (2011) Programmable nanowire circuits for nanoprocessors. Nature 470(7333):240–244
3. Pantano MF, Espinosa HD, Pagnotta L (2012) Mechanical characterization of materials at small length scales. J Mech Sci Technol 26(2):545–561
4. Haque MA, Espinosa HD, Lee HJ (2010) MEMS for in situ testing-handling, actuation, loading, and displacement measurements. MRS Bull 35(5):375–381
5. Hosseinian E, Pierron ON (2013) Quantitative in situ TEM tensile fatigue testing on nanocrystalline metallic ultrathin films. Nanoscale 5(24):12532–12541
6. Guo H, Chen K, Oh Y, Wang K, Dejoie C, Asif SAS, Warren OL, Shan ZW, Wu J, Minor AM (2011) Mechanics and dynamics of the strain-induced M1–M2 structural phase transition in individual VO2 nanowires. Nano Lett 11(8):3207–3213
7. Zhang Y, Liu XY, Ru CH, Zhang YL, Dong LX, Sun Y (2011) Piezoresistivity characterization of synthetic silicon nanowires using a MEMS device. J Microelectromech Syst 20(4):959–967
8. Zhang DF, Breguet JM, Clavel R, Sivakov V, Christiansen S, Michler J (2010) Electron microscopy mechanical testing of silicon nanowires using electrostatically actuated tensile stages. J Microelectromech Syst 19(3):663–674
9. Naraghi M, Ozkan T, Chasiotis I, Hazra SS, de Boer MP (2010) MEMS platform for on-chip nanomechanical experiments with strong and highly ductile nanofibers. J Micromech Microeng 20(12):125022
10. Brown JJ, Suk JW, Singh G, Baca AI, Dikin DA, Ruoff RS, Bright VM (2009) Microsystem for nanofiber electromechanical measurements. Sens Actuators a-Phys 155(1):1–7
11. Zhu Y, Espinosa HD (2005) An electromechanical material testing system for in situ electron microscopy and applications. Proc Natl Acad Sci USA 102(41):14503–14508
12. Haque MA, Saif MTA (2005) In situ tensile testing of nanoscale freestanding thin films inside a transmission electron microscope. J Mater Res 20(7):1769–1777
13. Kahn H, Ballarini R, Mullen RL, Heuer AH (1990) Electrostatically actuated failure of microfabricated polysilicon fracture mechanics specimens. Proc R Soc a-Math Phys Eng Sci 1999(455):3807–3823
14. Espinosa HD, Bernal RA, Minary-Jolandan M (2012) A review of mechanical and electromechanical properties of piezoelectric nanowires. Adv Mater 24(34):4656–4675
15. Espinosa HD, Bernal RA, Filleter T (2012) In situ TEM electromechanical testing of nanowires and nanotubes. Small 8(21):3233–3252
16. Espinosa HD, Zhu Y, Moldovan N (2007) Design and operation of a MEMS-based material testing system for nanomechanical characterization. J Microelectromech Syst 16(5):1219–1231
17. Abbas K, Alaie S, Leseman ZC (2012) Design and characterization of a low temperature gradient and large displacement thermal actuators for in situ mechanical testing of nanoscale materials. J Micromech Microeng 22(12):125027
18. Agrawal R, Peng B, Espinosa HD (2009) Experimental-computational investigation of ZnO nanowires strength and fracture. Nano Lett 9(12):4177–4183
19. Leach AM, McDowell M, Gall K (2007) Deformation of top-down and bottom-up silver nanowires. Adv Funct Mater 17(1):43–53

20. Johnston WG (1962) Yield points and delay times in single crystals. J Appl Phys 33(9):2716–2730
21. Dieter GE (1976) Mechanical metallurgy, 2nd edn. McGraw-Hill, New York
22. Chin GY, Hosford WF, Backofen WA (1964) Ductile fracture of aluminum. Trans Metall Soc Aime 230(3):437
23. Hsu TC, Littlejohn GS, Marchbank BM (1965) Elongation in the tension test as a measure of ductility. Proceedings Am. Soc. Testing Mats. 65:874
24. Wu ZX, Zhang YW, Jhon MH, Gao HJ, Srolovitz DJ (2012) Nanowire failure: long = brittle and short = ductile. Nano Lett 12(2):910–914
25. Sarraf EH, Cousins B, Cretu E, Mirabbasi S (2011) Design and implementation of a novel sliding mode sensing architecture for capacitive MEMS accelerometers. J Micromech Microeng 21(11):115033
26. Cui J, Guo ZY, Zhao QC, Yang ZC, Hao YL, Yan GZ (2011) Force rebalance controller synthesis for a micromachined vibratory gyroscope based on sensitivity margin specifications. J Microelectromech Syst 20(6): 1382–1394
27. Veryeri I, Basdogan I (2011) Adjusting the vibratory response of a micro Mirror via position and velocity feedback. J Vib Control 17(1):69–79
28. Vagia M, Koveos Y, Nikolakopoulos G, Tzes A (2010) Robust proportional-integral-derivative controller design for an electrostatic micro-actuator with measurement uncertainties. IET Control Theory Appl 4(12):2793–2801
29. Koo BJ, Zhang XM, Dong JY, Salapaka SM, Ferreira PM (2012) A 2 degree-of-freedom SOI-MEMS translation stage with closed-loop positioning. J Microelectromech Syst 21(1):13–22
30. Zhu Y, Corigliano A, Espinosa HD (2006) A thermal actuator for nanoscale in situ microscopy testing: design and characterization. J Micromech Microeng 16(2):242–253
31. Zhu Y, Moldovan N, Espinosa HD (2005) A microelectromechanical load sensor for in situ electron and x-ray microscopy tensile testing of nanostructures. Appl Phys Lett 86(1):013506
32. Filleter T, Ryu S, Kang K, Yin J, Bernal RA, Sohn K, Li SY, Huang JX, Cai W, Espinosa HD (2012) Nucleation-controlled distributed plasticity in penta-twinned silver nanowires. Small 8(19):2986–2993
33. Bernal RA, Agrawal R, Peng B, Bertness KA, Sanford NA, Davydov AV, Espinosa HD (2011) Effect of growth orientation and diameter on the elasticity of GaN nanowires. a combined in situ TEM and atomistic modeling investigation. Nano Lett 11(2):548–555
34. Qin QQ, Zhu Y (2013) Temperature control in thermal microactuators with applications to in situ nanomechanical testing. Appl Phys Lett 102(1):013101
35. Hopcroft MA, Nix WD, Kenny TW (2010) What is the Young's modulus of silicon? J Microelectromech Syst 19(2):229–238
36. Okada Y, Tokumaru Y (1984) Precise determination of lattice-parameter and thermal-expansion coefficient of silicon between 300 and 1500-K. J Appl Phys 56(2):314–320
37. Li L, Begbie M, Brown G, Uttamchandani D (2007) Design, simulation and characterization of a MEMS optical scanner. J Micromech Microeng 17(9):1781–1787
38. Miller DC, Boyce BL, Dugger MT, Buchheit TE, Gall K (2007) Characteristics of a commercially available silicon-on-insulator MEMS material. Sens actuators a-Phys 138(1):130–144
39. Bao M (2005) Analysis and design principles of MEMS devices. Elsevier, Amsterdam
40. Yamahata C, Collard D, Legrand B, Takekawa T, Kunternura M, Hashiguchi G, Fujita H (2008) Silicon nanotweezers with subnanometer resolution for the micromanipulation of biomolecules. J Microelectromech Syst 17(3):623–631
41. MEMSCAP (2011) SOIMUMPS design handbook, Rev. 7. http://www.memscap.com/en_mumps.html. Accessed July 2013
42. Ogata K (2008) Modern control engineering, 3rd edn. Prentice-Hall, Upper Saddle River
43. Agrawal R, Peng B, Gdoutos EE, Espinosa HD (2008) Elasticity size effects in ZnO nanowires-A combined experimental-computational approach. Nano Lett 8(11): 3668–3674
44. Gao YJ, Fu YQ, Sun W, Sun YL, Wang HB, Wang FY, Zhao JW (2012) Investigation on the mechanical behavior of fivefold twinned silver nanowires. Comput Mater Sci 55:322–328
45. Wu JY, Nagao S, He JY, Zhang ZL (2011) Role of fivefold twin boundary on the enhanced mechanical properties of fcc Fe nanowires. Nano Lett 11(12):5264–5273
46. Cao AJ, Wei YG (2006) Atomistic simulations of the mechanical behavior of fivefold twinned nanowires. Phys Rev B 74(21):214108